Real-time laser spot modulation in Laser Powder-Directed Energy Deposition via wobbling: A path to superior 316L stainless steel components

Journal of Materials Research and Technology 36 (2025) 8462–8474

Contents lists available at ScienceDirect

Journal of Materials Research and Technology

journal homepage: www.elsevier.com/locate/jmrt

Real-time laser spot modulation in Laser Powder-Directed Energy Deposition via wobbling: A path to superior 316L stainless steel components

Stefano Felicioni [a,*], Alberta Aversa [a,b], Erica Librera [c], Mariangela Lombardi [a,b], Federica Bondioli [a,b]

[a] Department of Applied Science and Technology, Politecnico di Torino, Corso Duca degli Abruzzi 24, 10129, Torino, Italy
[b] Consorzio Interuniversitario Nazionale per la Scienza e Tecnologia dei Materiali (INSTM), Via G. Giusti 9, 50121, Firenze, Italy
[c] Prima Additive s.r.l., C.so Re Umberto 54, 10128, Torino (TO), Italy

ARTICLE INFO

Handling Editor: L Murr

Keywords:
Additive manufacturing
Laser
Directed energy deposition
Steel
316 L
Oscillating strategy
Laser wobbling
Building rate
Phase transformation
Microstructure
Mechanical properties

ABSTRACT

Achieving high-quality Laser Powder-Directed Energy Deposition (LP-DED) components require the precise tuning of process parameters such as laser power, scanning speed, and laser spot size. Among these, laser spot size is a particularly critical factor. The use of a large spot size led to high building rate and process efficiency at the expense of surface finish and geometrical accuracy. This investigation aimed to understand how a variable laser spot affects the thermal history of LP-DED AISI 316L stainless steel components and consequently their microstructure and mechanical properties. The study first examined the effects of the laser spot and sample geometry on the microstructural features using optical microscopy (OM), scanning electron microscopy (SEM), electron backscatter diffraction (EBSD) and X-ray diffraction (XRD). Secondly, the characterization of mechanical properties was conducted via tensile tests and the effects of the variable laser spot on ductility and on the various strengthening mechanisms were analysed. The results revealed that using a larger laser spot leads to heat accumulation, which becomes especially crucial when depositing geometries characterized by a small cross section. These findings lay the groundwork for enhancing the LP-DED process efficiency in a more viable manner taking advantage of the different solidification conditions.

1. Introduction

Laser Additive Manufacturing (LAM) comprises a variety of processes for creating three-dimensional metallic components layer by layer using a laser. Among LAM techniques, Laser Powder-Directed Energy Deposition (LP-DED) is particularly suitable for producing large parts with a high strength-to-weight ratio and minimal material waste [1,2].

This has led to the widespread adoption of LP-DED in disparate industries such as aerospace, petrochemical, automotive, power generation and heavy-duty applications such as tooling in the context of injection dies [3].

In a LP-DED process, the powder is delivered onto a substrate surface through a single or multiple nozzles within a local inert atmosphere. A high-power laser beam provides the necessary energy to melt the powder, which is then delivered into the molten pool [4].

Achieving high-quality LP-DED components necessitates the precise tuning of various processing parameters. These parameters include laser power (P), scanning speed (SS), powder feed rate (f), hatching distance (Hd), Z-step (dZ), scanning strategy and laser spot size (Ls) [5]. Compared to powder bed additive manufacturing techniques, the size of the laser spot and consequently of the molten pool in LP-DED processes is over an order of magnitude larger, typically in the millimeter range. Consequently, LP-DED components tend to have a higher build rate but poorer surface finish and lower geometrical accuracy with respect to parts produced by powder bed processes.

To address these issues, recent research has focused on developing deposition heads with sub-millimeter laser spots to enhance surface quality and precision at the expense of the deposition rates [6]. Because of this reason there is a strong interest in developing variable laser spot in order to reach good surface quality where needed and high deposition rates where the surface quality is not relevant. To the authors knowledge, there are no commercially available variable spot systems,

* Corresponding author.
E-mail address: stefano.felicioni@polito.it (S. Felicioni).

https://doi.org/10.1016/j.jmrt.2025.05.049
Received 26 February 2025; Received in revised form 6 May 2025; Accepted 6 May 2025
Available online 14 May 2025

resulting in a significant gap in the literature.

The variation in the molten pool size is also a crucial parameter in other additive technologies, such as electron beam powder bed fusion (EB-PBF), where homogenization of the microstructure can be achieved by varying the degree of beam collimation [7]. However similar applications on laser-based AM process are conspicuously lacking due to the great difficulties in managing different apertures of the optical chain when high powers are adopted [8].

In this context, laser oscillation, commonly referred to as laser wobbling, offers a particularly promising approach for achieving real-time spot size variation by creating a larger apparent spot. This technique has been widely applied in laser welding and has recently gained attention in additive manufacturing. Aversa et al. [9], demonstrated its effectiveness in LP-DED, achieving nearly fully dense 316L cubes through proper tuning of process parameters. Similarly, Gong et al. [10] showed that laser oscillation can significantly refine the microstructure of 316L produced using a wire-arc additive manufacturing (WAAM) setup; additionally, Huang et al. [11] demonstrated that laser wobbling can reduce surface roughness in cubic samples fabricated with a self-developed laser powder bed fusion (L-PBF) system.

Although the literature on laser wobbling in additive manufacturing remains limited, findings from welding research consistently highlight that this strategy not only alters the size and shape of the molten pool but also significantly influences the resulting microstructure and material properties. In particular, literature results showed that wobbling reduces the hardness of the heat-affected zone, the content of brittle phases, and melt pool emissions of spatters and slug [12]. Kuryntsew et al. [13] reported that the use of wobbling on structural stainless steels causes lower cooling rates and minimizes the number of detrimental phases providing greater ductility. Voropaev et al. [14] described the effects of the adoption of the oscillation strategy in the welding of 316L and showed how it caused a δ-ferrite increase and consequently higher strength. De Oliveira et al. [15] demonstrated the benefits of wobbling in 316L welding, attributing them to an increased melt pool area and to the high width to depth ratio of the bead.

AISI 316L is among the most used alloys in additive manufacturing and 316L LP-DED components are nowadays recognized as valid alternatives to the conventional manufacturing also for medium batch production [16]. The processability, microstructure, and properties of 316L stainless steel fabricated through LP-DED have been widely investigated [17,18]. Research highlights reveal that this material is easily processable by LP-DED, achieving relative densities up to 99.9 % [19,20]. The microstructure of 316L LP-DED components predominantly feature large columnar grains and fine austenitic cells, which are surrounded by small amounts of retained δ–ferrite [21]. This distinctive microstructure arises from the rapid and directional cooling of LP-DED, typically ranging from 10^3 to 10^4 K/s. Nonetheless, numerous studies have demonstrated that various factors and process parameters significantly influence these microstructural features and consequently the mechanical properties of 316L LP-DED components. For instance, Shamsaei et al. [22] found that both strength and elongation of LP-DED 316 components are substantially influenced by the inter-layer time interval that is function of the dimension of the layer deposited. A big cross section, having long intervals, leads to high solidification rates, steep thermal gradients, and fine microstructures reflecting high strength and a lower ductility. Research conducted by Ma et al. [23] demonstrated that the tensile strength and the elongation of 316L LP-DED samples are mostly related to the scanning speed employed during fabrication. Xu et al. [24] considered also the overlap ratio as an impacting parameter on the mechanical properties and grain morphology. These analyses clearly underlines that the impact of process parameters on 316L LP-DED properties is primarily due to the different thermal history experienced by the material, specifically to the melt pool thermal gradient, together with the Intrinsic Heat Treatment (IHT) to which the deposited material undergoes due to the deposition of the subsequent layers.

However, despite the significant influence of the laser spot variation on the microstructure of LP-DED parts, this area remains still underexplored. The present study aims to address this existing gap in the literature by thoroughly investigating the effects of the real time laser spot size variation on the microstructural features and mechanical properties of 316L stainless steel components produced by LP-DED on a submillimeter set-up, paving the way for improved component quality and performance.

2. Experimental procedures

A pre-alloyed 316L gas atomized powder with a particle size distribution in the range $15-45\ \mu m$, supplied by Carpenter Additive (Carpenter Technology Corporation, PA US), was used as raw material to produce all the samples. The chemical composition of the powder, measured by the powder provider, is detailed in Table 1.

The experiments were conducted on a test bench featuring a 3-axis CNC machine developed by Prima Additive S.p.A. This system was equipped with a commercial nozzle with 0.7 mm laser spot deposition head and an IPG YLS-3000 Ytterbium-doped fibre laser with a maximum power of 3 kW and a central wavelength of 1070 nm. Vertical and horizontal parallelepiped shaped samples were built with the conventional and with the oscillating laser spots with two sets of optimal process parameters, outlined in Table 2. These parameters were selected after optimization to achieve near-complete material densification with a fixed energy density (E_d) of 100 J/mm^2, defined as:

$$E_d = \frac{P}{SS \cdot L_s}. \quad \text{(Eq. 1)}$$

These samples were designated as W_V, NW_V, W_H, NW_H, where W stands for wobbling and NW for non-wobbling condition, while the subscripts 'H' and 'V' denote the horizontal and vertical orientations of the samples, respectively (Fig. 1a). Key parameters in the LP-DED process for characterizing the oscillating scanning strategy include the oscillation diameter (do) and oscillation frequency (fs) which express the number of rotations in the unit of time. Fig. 1b illustrates the laser pattern in wobbling motion. For both scanning conditions, the deposition strategy involves bi-directional raster scanning with a 90° interlayer rotation. The selected amplitude allows to reach a virtual laser spot of 1,1 mm which correspond to a 60 % increment with respect to the real spot size.

The LP-DED samples density was measured using the Archimedes principle in line with the ASTM B-311 [25] test procedure using a KERN ABS 80-4 N (KERN & SOHN GmbH, Germany) having a resolution of 0.10 mg, equipped with the density measurement setup KERN YDB-03. The relative density was calculated using the density of the powder as the reference. The effect of the oscillation on the process was evaluated in terms of building rate (BR) and powder efficiency (η), defined as:

$$BR = \frac{V_{th}}{t} \quad \text{(Eq. 2)}$$

$$\eta = \frac{f}{BR^* \rho} \quad \text{(Eq. 3)}$$

where V_{th} is the theoretical volume of the samples, t is the building time, f is the powder feed rate and ρ is the density of the material.

The samples were then cut along the XY and XZ planes, mounted and polished according to standard metallographic methods up to 0,06 μ m alumina suspension. All specimens were then etched using Marble etchant (a solution of 4 g $CuSO_4$ in 20 ml HCl and 20 ml water) for 10 s. Melt pools shape, microstructure morphology and phase distribution were examined using a LEICA DMI 5000 M Optical Microscope (Leica Microsystems GmbH, Germany), a TESCAN s9000G (Tescan Group a.s., Czech Republic) FE-SEM (Field Emission Scanning Electron microscopy) with EBSD (Electron Backscattered Diffraction), and a Thermo-Fisher Phenom XL G2 (Fisher Scientific Co., MA, USA) benchtop SEM with

Table 1
Measured 316L powder chemical composition.

Fe	Mo [wt. %]	N [wt. %]	C [wt. %]	Cr [wt. %]	Mn [wt. %]	S [wt. %]	Ni [wt. %]	Si [wt. %]	P [wt. %]	O [wt.%]
Bal.	2,5	0,10	0,02	17,00	1,50	0,03	11,00	0,5	0,04	0,10

Table 2
Building parameters used in LP-DED process with a fixed real energy density of 100 J/mm^2 (P = laser power; SS = scanning speed; f = powder feed rate; Hd = hatching distance; dZ = Z-step, do = oscillation diameter, fs = oscillation frequency).

Sample code	P [W]	SS [mm/min]	f [g/min]	Hd [mm]	dZ [mm]	do [mm]	fs [Hz]	Apparent energy density [J/mm^2]
W_V	600	515	3,5	1,11	0,25	0,45	167	60
NW_V	500	430	3,5	0,6	0,35	–	–	–
W_H	600	515	5	1,11	0,25	0,45	167	60
NW_H	500	430	5	0,6	0,35	–	–	–

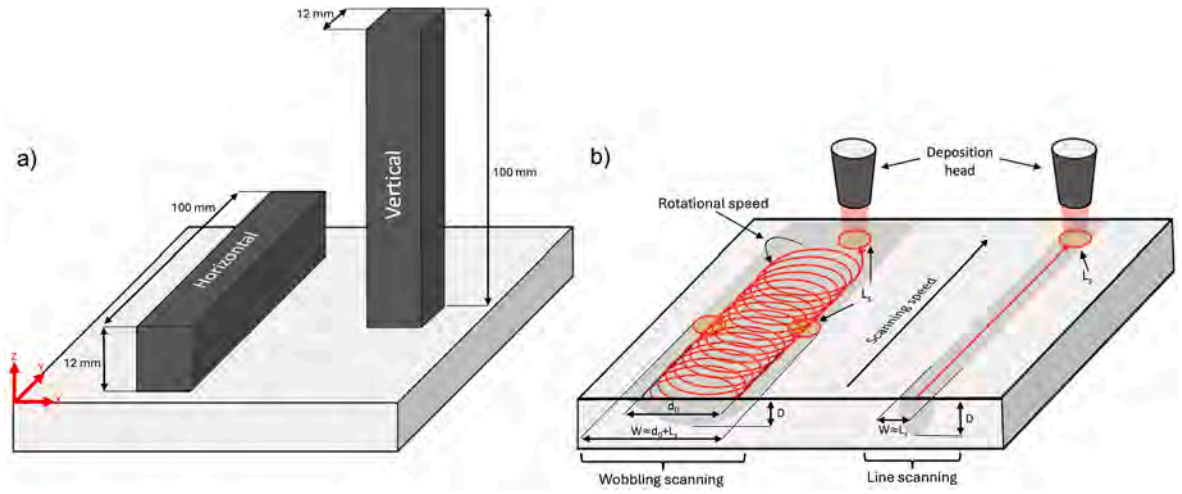

Fig. 1. a) Overview of the geometries of the samples built in in the current work; b) Schematic representation of the "wobbling scanning" compared to the conventional "line scanning".

EDS (Energy Dispersive Spectroscopy). EBSD analysis was conducted at 20 keV, 10 nA, with a step size of 0,2 μm; Si standard was used for the calibration of the equipment. Primary Cellular Arm Spacing (PCAS) was measured on etched samples OM images using a proprietary MATLAB image analysis toolbox, utilizing the triangle technique. PCAS values were used to estimate cooling rates and investigate the different thermal history of the material in each experimental condition.

The relation between the cooling rate, $\dot{T}$ and the PCAS is described by the following equation [26]:

$$PCAS = 80\dot{T}^{-0,33} \quad \text{(Eq. 4)}$$

Phase content was determined by X-ray diffraction (XRD) analysis on the plane perpendicular to the building direction, using an Empyrean diffractometer (Malvern Panalytical Ltd., UK) with Cu-Kα radiation. The setup operated at 40 kV and 40 mA with a step size of 0.013° over the 2θ range from 30 to 100° after proper calibration with LaB_6 standard specimen, and X-Pert High Score software was used for deconvolution and integration of XRD patterns.

To assess the mechanical performance and plastic behaviour, tensile tests were conducted on specimens machined from parallelepiped samples. The tensile specimens conformed to ASTM E8-M [27] standards for powder metallurgy samples. To evaluate the anisotropy, these samples were oriented both perpendicular and parallel to the build direction. Four specimens per condition were tested at room temperature using a Zwick-Roell Z050 servo-hydraulic testing machine, equipped with a 50 kN load cell, at 10^{-3} s^{-1} [27].

3. Results and discussion

A comparison between build rate and powder efficiency of W and NW samples in both the deposition orientations is presented in Fig. 2. The oscillating scanning strategy enhanced productivity and efficiency of about 40 % and 55 % respectively. Concerning the densification degree, all the samples showed less than 0.5 % porosity (Table 3). In all cases the residual porosity is spherical and measures only a few microns in diameter. The higher porosity detected in the samples built with the wobbling strategy, could be due to the larger molten pool (Fig. 1b) which is more susceptible to gas entrapment.

3.1. Microstructural characterization

The microstructures of each condition are depicted in Figs. 3 and 4 for the horizontal and vertical orientation respectively, showcasing both the parallel plane (Z ↑) and the perpendicular plane to the building direction (Z ⊙). Starting with the horizontal samples, W_H condition reveals layers composed of numerous molten pools due to the rapid laser oscillations (Fig. 3a and b), whereas the NW_H specimen exhibits deep and thick tracks characteristic of the standard LP-DED deposition strategy (Fig. 3c and d). It is interesting to note from the meltpool depth measure that the W_H sample is also characterized by thinner layers (300 μm) than the NW_H ones (500 μm). This could be due, on the one hand, to the lower dZ used during the building process and, on the other hand, to the larger apparent laser spot size that leads to an apparent energy density lower than the real one. As a result, the molten pools have a higher surface-to-volume ratio leading to different solidification conditions.

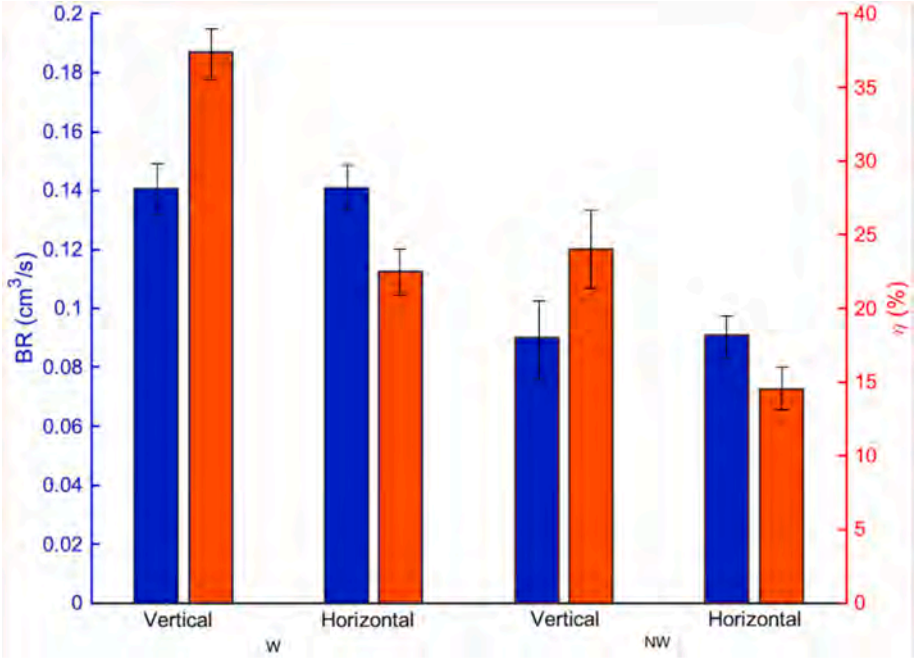

Fig. 2. Process comparison between the conventional and wobbling scanning strategy in terms of building rate and powder efficiency.

Table 3
Archimedes relative density of the deposited samples.

Sample Code	W_V	NW_V	W_H	NW_H
Relative Density	99.64 ± 0.02 %	99.86 ± 0.01 %	99.77 ± 0.02 %	99.93 ± 0.01 %

Similar observations can be made also for the vertical samples (Fig. 4); however, in this case, a deeper penetration of the molten pools (approximately the 15 % greater in depth) can be noted compared to the horizontal counterparts further underscoring the process-induced differences in melt pool behavior.

This feature, which is particularly evident in the W_V sample (Fig. 4a and b), can be attributed to the higher heat accumulation of samples characterized by a small cross section which has been demonstrated by numerous thermal models and experimental studies on LP-DED available in the literature [28,29]. In LP-DED, in fact, the cooling process is primarily governed by conduction, following the integral form of Fourier's law:

$$Q = \int_A q \cdot dA \cdot \Delta t \quad \text{(Eq. 5)}$$

which expresses a direct proportionality between heat transfer (Q) and the surface area (A) involved in the heat exchange.

Additionally, the oscillating scanning strategy, characterized by a higher BR, reduces the inter-layer cooling time, which further impedes an effective thermal transfer. This slower heat dissipation in vertical samples leads to a gradual increase in the temperature of previously deposited layers as the deposition progresses. Because of these reasons, in the vertical samples, when a new layer is deposited on the previous one, which is already at a high temperature, it causes its remelting resulting in a higher layer thickness.

A closer examination of the samples microstructure reveals that, in both W and NW samples, the rapid cooling and directional solidification of the LP-DED process result in coarse columnar grains (Supplementary 1) composed of γ-dendrites in the form of micrometric cells (Fig. 5). A comparison of the micrographs indicates that the NW samples, in both orientations (Fig. 5c and d), exhibit a co-existence of columnar-dendritic and equiaxed-dendritic structures, whereas the predominant morphology in the W samples is the equiaxed-dendritic (Fig. 5a and b). These microstructures can be explained by considering the thermal gradient (G) and the liquid to solid transition velocity (R) during the solidification process. The interplay of these factors determines, in fact, the morphology (G/R) and the size (G•R) of the resulting microstructure [30,31]. In general, low G/R values result in equiaxed structures, while high G/R values lead to the formation of columnar dendrites. In the case of the NW configuration, the presence of both morphologies is associated with different G/R values in various melt pool zones. At the melt pool border, during the initial stages of solidification, solid conduction predominates, resulting in a high temperature gradient and a low liquid to solid velocity [32,33]. Consequently, high G/R values are achieved, leading to the formation of a columnar-dendritic microstructure. As the solidification progresses, in the melt pool center, convection overtakes conduction as the primary heat transfer mechanism, causing an increase in R and a decrease in G, which results in the transition from columnar to an equiaxed microstructure.

On the contrary, the employment of the oscillating scanning strategy in the W samples significantly reduces the thermal gradient among the layers thanks to the higher build rate and lower inter-layer cooling time. This results in relatively constant and low G/R values, which manifest as an exclusively equiaxed dendritic microstructure that only varies in size across different areas of the layer.

The calculation of the Primary Cell Arm Spacing (PCAS) confirmed the different cooling rates. The analysis demonstrated how the virtual increase of the spot size impacts the cooling rate, slowing it down from $8{,}7 \bullet 10^3$ K/s to $8{,}2 \bullet 10^3$ K/s in the horizontal orientation and from $17{,}1 \bullet 10^3$ K/s to $3.1 \bullet 10^3$ K/s in the vertical one.

To further characterize the microstructures of the samples, EBSD analyses were conducted. Fig. 6 presents the IPF maps for each sample on the XY plane, with the relative grain size (GS), measured by the equivalent circle diameter, detailed in Table 4. The GS values of the NW samples are not influenced by the sample orientation. For the standard scanning deposition, the growth of the columnar grain typically starts at the boundary of the track and ends at its centerline, as clearly shown in Fig. 6c and d. This solidification pattern can be attributed to the well-known phenomenon in LAM and welding where, thanks to the rapid and strongly directional solidification, grains grow along the heat

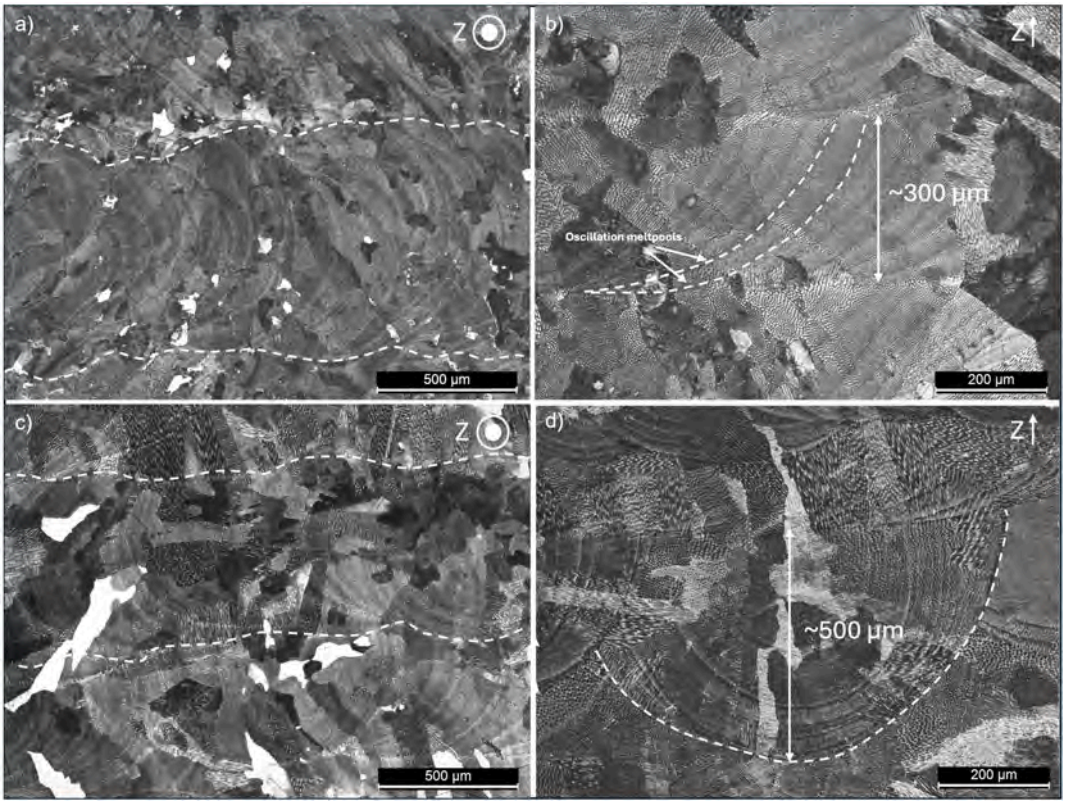

Fig. 3. Optical micrographs along XZ and XY planes of a-b) W_H sample displaying interconnected molten pools and the oscillatory laser patterns; c-d) NW_H showing conventional deeper molten pool with columnar grain growth following the building direction.

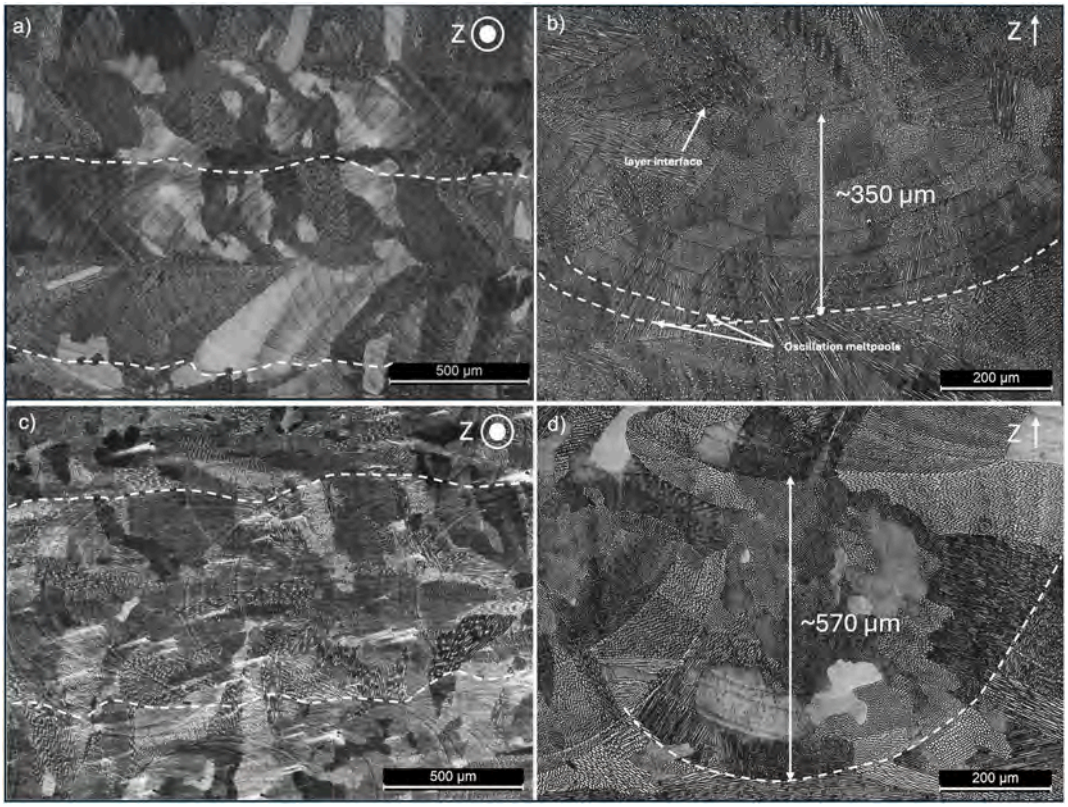

Fig. 4. Optical micrographs along XZ and XY planes of a-b) a W_V sample displaying interconnected molten pools and the oscillatory laser patterns and c-d) a NW_V sample showing higher penetration of the molten pool with large grains following the building direction.

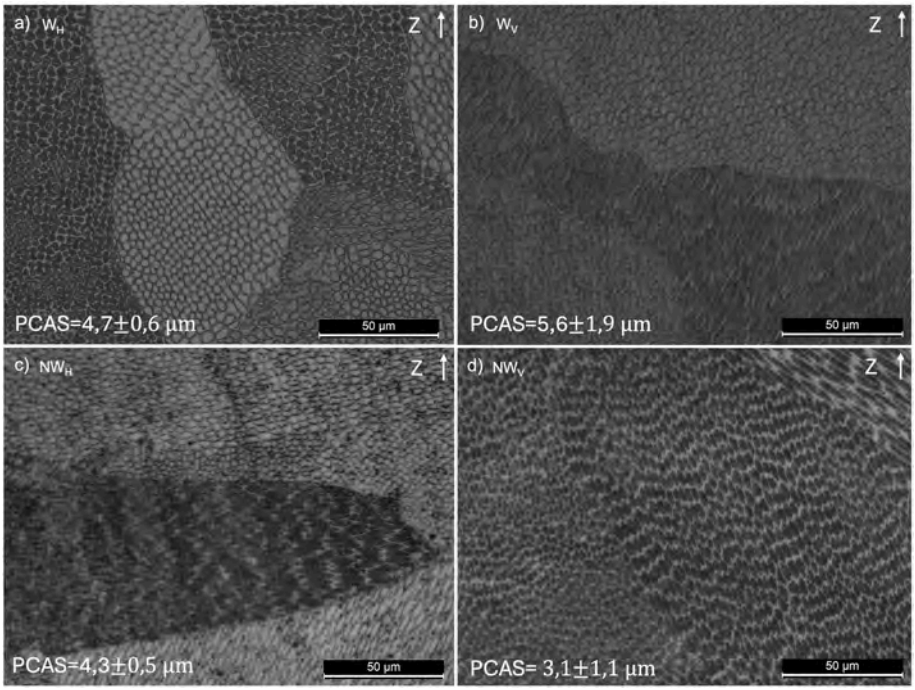

Fig. 5. Representative optical micrographs along the XZ cross section at 200× magnification displaying the $\gamma - Fe$ equiaxed dendrites and relative PCAS values of the obtained samples.

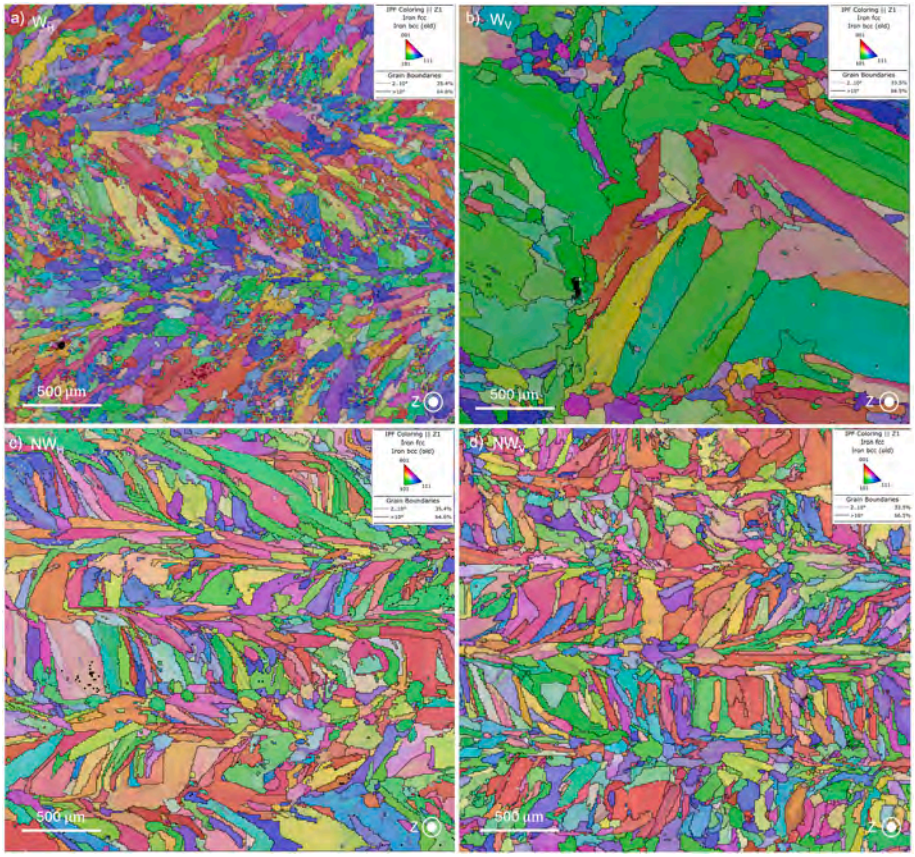

Fig. 6. EBSD IPF + grain boundary maps of the analysed samples on the plane perpendicular to the building direction (XY): a) W_H; b) W_V; c) NW_H; d) NW_V.

extraction direction [34].

Regarding laser wobbling, instead, compared to the NW condition, fine grains are observed in the W_H sample, while coarse grains are detected in the W_V specimen. This outcome can be understood by examining the microstructure of W_H sample, where a mixture of large columnar grains and small equiaxed grains is present at the melt pool

Table 4
Grain size of the analysed samples.

Sample code	Counted grains	GS [μm]
W_V	268	156 ± 46
NW_V	882	85 ± 16
W_H	1161	68 ± 11
NW_H	696	92 ± 24

boundaries. This result could be attributed to the initial columnar grain growth followed by dendritic fragmentation due to the stirring of the flow caused by the rotary laser scanning pattern. Similar conclusions were drawn by Zhao et al. [35] in their study on laser wobbling welding of an aluminum alloy.

If this solidification mechanism is transferred in the context of the vertical orientation of the Wv sample, the significant heat accumulation with the ongoing of the deposition, extensively described in previous sections, becomes a key factor for solid-state grain growth of the fine grains created during the meltpool solidification. The growth of these fine structures is energetically favored and thus, similarly to recrystallization, they overgrow all the initial grains, resulting in a very coarse microstructure. The EBSD maps suggest slight texture differences; however, using EBSD, it is challenging to evaluate these differences especially in Wv sample due to the large grain size.

To achieve a comprehensive comparison, XRD analysis was performed on the XY plane (Fig. 7). Comparing the patterns with the reference for γ-Fe, the NW_H sample exhibits a random grain distribution (i.e., no texture), W_H sample shows a slight <022> texture, while both vertical samples (NW_V and W_V) exhibit a <111> texture, indicating a strong directional cooling that is consistent with the results obtained from the PCAS measurements.

It is well-known that grain boundaries in polycrystalline materials can be categorized into low-angle and high-angle grain boundaries. Low-angle grain boundaries (LAGBs), defined by a misorientation angle of less than 15°, can be considered as an array of dislocations that globally contribute to enhanced strain hardening capabilities of the material. In contrast, high-angle grain boundaries (HAGBs), which have misorientation angles exceeding 15°, play a crucial role in preventing the propagation of brittle cracks [36]. The steep temperature gradients and rapid cooling rates inherent to LP-DED lead to a non-equilibrium solidification process in the molten pool, often resulting in the formation of numerous LAGBs [29]. As illustrated in Fig. 6, the presence of LAGBs is consistent across all experimental conditions. To further evaluate these aspects, the dislocation density, ρ_0, can be accurately quantified using the Kernel Average Misorientation (KAM) angle extracted from the maps in Fig. 8 and summarized in Fig. 9 using the following equation [37]:

$$\rho_0 = \frac{2\theta_{KAM}}{bd} \quad \text{(Eq. 6)}$$

where b is the Burger vector (assumed to be 0.25 nm for austenite [38]) and d is the step size employed in the EBSD measurements. The numerical calculations of ρ_0 (Fig. 9) show a high dislocation density in horizontal samples, with the highest value attained in the W_H condition. The intricate dislocation network recorded in these samples is in line with the efficient heat dissipation characteristic of this condition.

Regarding the vertical samples due to the complex thermal history in the solid state, the dislocation density decreases.

3.2. Phase content

It is well-established that AISI 316L can retain a certain quantities of δ-ferrite when processed using additive manufacturing techniques [29,39,40] and that the presence of this phase can strengthen the ductile austenitic matrix [39]. Evidence ofδ-ferrite retention in both W and NW samples can be observed in the XRD patterns shown in Fig. 7b, where traces of the main intensity peak (2θ = 44.3° [16,41]) of this crystallographic phase are present. Due to the extremely limited presence of δ-ferrite, its quantification and analysis were performed through a statistical evaluation of EBSD phase maps acquired at multiple magnifications and across different sample regions. The phase content, illustrated in Fig. 10 alongside representative phase maps, show that in all conditions, ferrite tends to form along the grain boundaries. Additionally, there is a correlation between the oscillating scanning strategy, the sample orientation, and the ferrite content. Notably, higher ferrite content is detected in the NW samples, particularly in the NW_H sample less susceptible to heat accumulation.

The primary factors influencing theδ-ferrite content are chemical composition, cooling rate, and heat treatment. In stainless-steel, in fact, the understanding of the solidification phenomena can be done considering the pseudo-binary and the Schaeffler diagram in which the phase contents is represented as a function of the Chromium Equivalent (Cr_{eq}) and Nickel Equivalent (Ni_{eq}) values [42]. Higher Cr_{eq} values or lower Ni_{eq} values increase the likelihood of formingδ-ferrite as the primary phase, resulting in moreδ-ferrite retained at room temperature. The rapid cooling limits the austenite growth due to slower diffusion, thereby leading to a higher retainment ofδ-ferrite. Finally, the heat

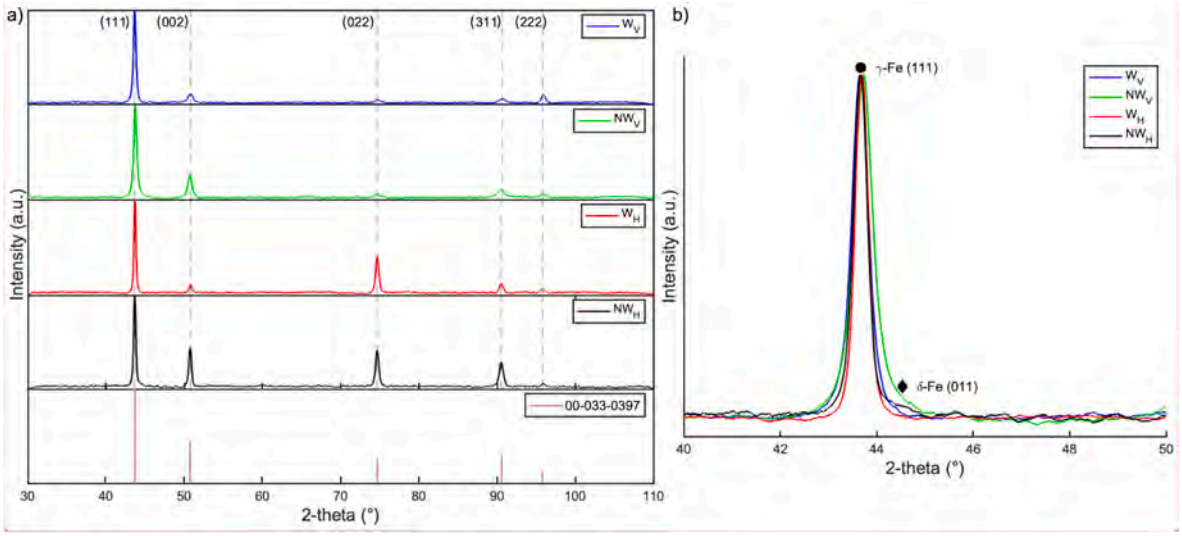

Fig. 7. a) XRD patterns of the samples acquired on the XY plane showing the (111) texture of W_V and W_H; b) inset of a) between 40 and 50°.

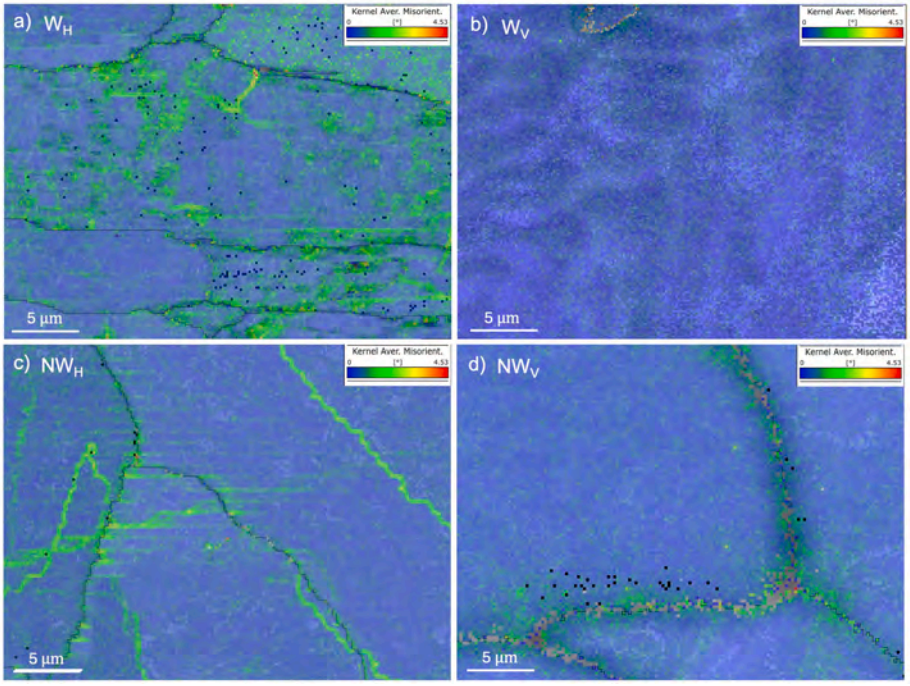

Fig. 8. High magnification KAM maps displaying the local misorientation in the crystal lattice used for the calculation of the dislocation density of the 316L samples. Numerical data related to these images are reported in Fig. 9.

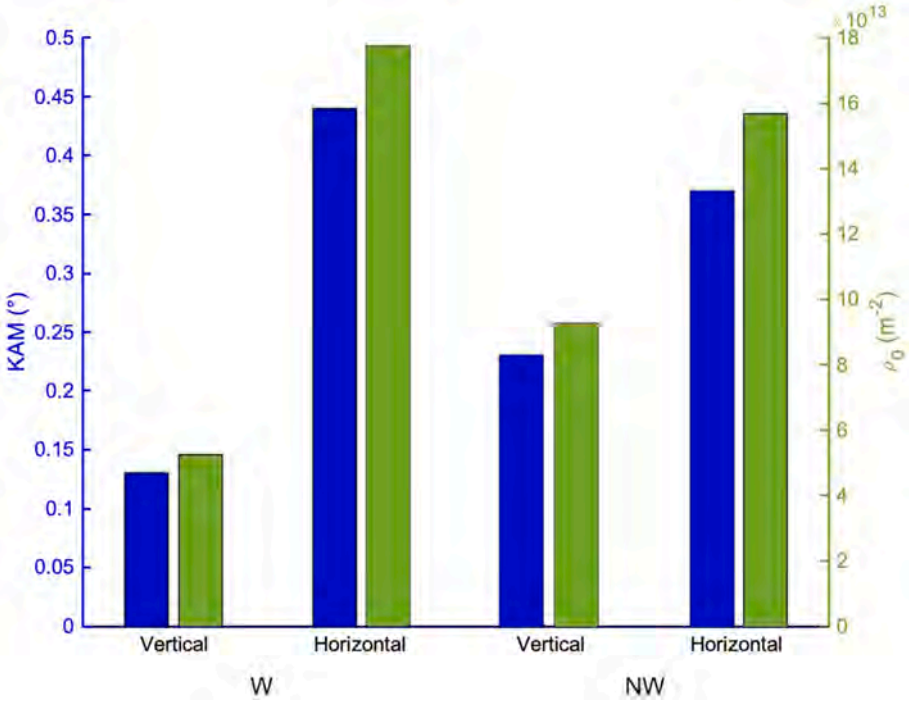

Fig. 9. KAM average values comparison and dislocation density between the conventional and wobbling scanning strategy.

treatment reduces the ferrite content enhancing the diffusion rate of the alloying elements, promoting the growth of the austenite phase [43].

In this study, the 316L alloy composition resulted in a Cr_{eq} of 20.25 % and a Ni_{eq} of 12.35 %, which, based on the Shaffer diagram, suggests a maximum retention of 5 % ferrite in all samples. In the samples under investigation, a relevant ferrite content is expected to be retained during solidification due to the high cooling rate. This is confirmed by EDS maps, that reveal the segregation of ferrite stabilizers (Cr, Mo, Si) at the cell boundaries (Fig. 11). This localized alteration in chemical composition modifies the local ratio of Cr_{eq}/Ni_{eq}, thereby promoting the stabilization of ferrite at the cell boundaries [44]. In the solid material, the ferrite content is then reduced during the building process thanks to the continuous heating due to the deposition of subsequent layers.

To validate the role of the LP-DED Intrinsic Heat Treatment (IHT) on the ferrite content, SEM images of the ferrite were taken because there is a correlation between the δ-phase morphology (i.e. vermicular, skeletal

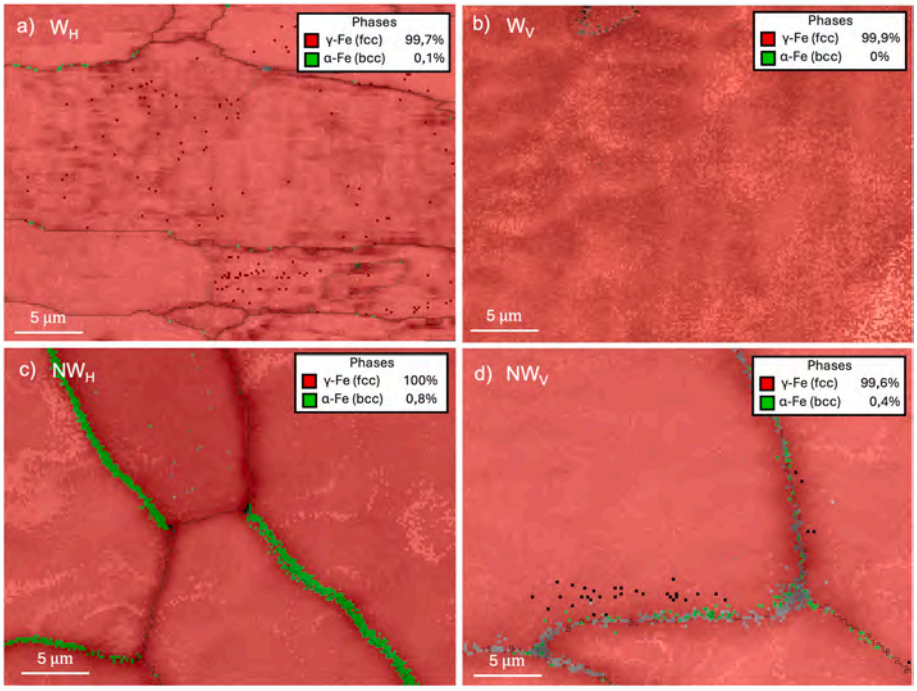

Fig. 10. High magnification phase maps displaying the austenite-ferrite (AF) solidification mode induced by the LP-DED process in the samples. The reported composition is averaged on a statistic on different areas of the sample.

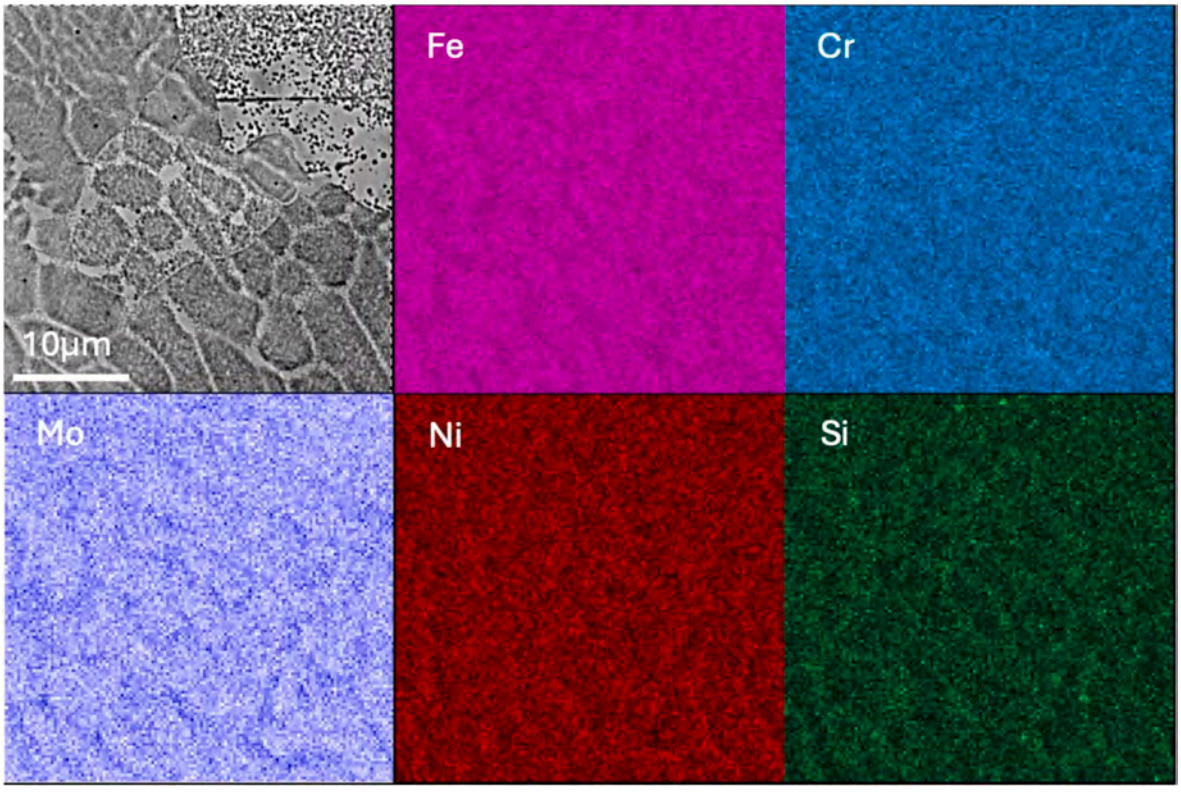

Fig. 11. Compositional EDS maps of the NW_H sample, displaying the cell boundaries in the LP-DED 316L SS blocks are depleted in Fe and Ni and enriched in Cr, Mo, and Si.

and lathy) and the mechanism that leads to its retainment [45].

In the current study, only the skeletal morphology was detected from the FESEM analysis, as shown in the representative micrograph of Fig. 12 relative to the NW_H sample. This conclusion points out that, while the chemical composition and cooling rate are influencing the ferrite retainment during solidification, the IHT is the main factor in the δ phase refinement. As a matter of facts, when the already deposited layers are reheated due to the deposition of the following ones, the

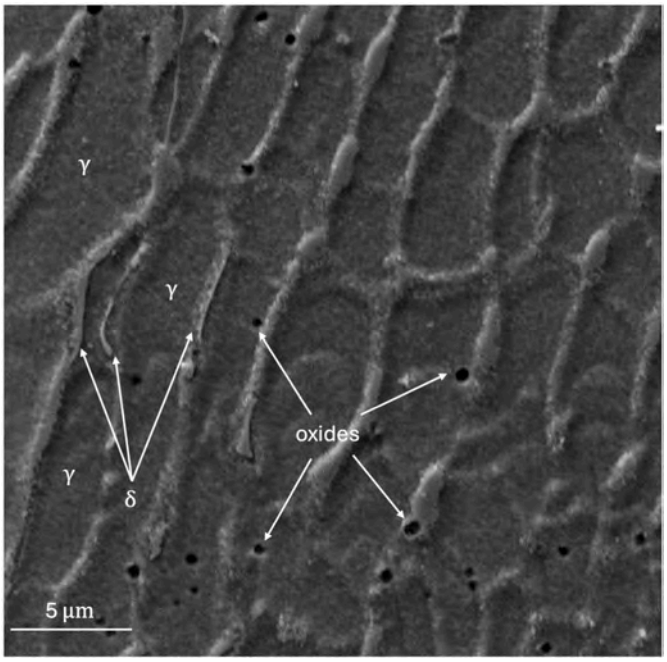

Fig. 12. Representative SEM micrograph showing the skeletal morphology of δ-ferrite along the cell borders of the NW_H sample, indicating an austenite-ferrite (AF) solidification mode due to the material reheating.

austenite continue to grow and the lathy ferrite acquires the skeletal shape [45]. Additionally, Fig. 12 shows an oxide dispersion predominantly at the cell boundaries, a common characteristic of 316L components processed via LP-DED [16,31].

3.3. Mechanical properties

Fig. 13 presents a summary of the mechanical properties of all the samples. The representative tensile curves reveal a significant anisotropy between the two deposition orientations, which becomes even more pronounced with the use of laser wobbling. In the horizontal deposition, the W_H samples exhibit the highest ultimate tensile strength (UTS) of 672 ± 13 MPa, accompanied by the lowest elongation (El.) of 28 ± 3 %. Conversely, the W_V samples, show the highest elongation of 60 ± 2 %, while their UTS drops to a minimum of 517 ± 6 MPa. For the NW samples, the scattering between the two deposition orientations is less pronounced. NW_H samples display a UTS of 639 ± 2 MPa and an El. of 31 ± 2 %, while NW_V samples have a UTS of 581 ± 1 MPa and an El. of 40 ± 1 %. It is interesting to notice that all the listed properties are higher than the standards of ASTM A479 [46] which reports UTS and YS of 485 MPa and 170 MPa respectively, for the mechanical performances of stainless steels in the context of high-pressure applications. The observed anisotropy may be attributed to the well-documented presence of columnar grains (Supplementary 1) in LP-DED components, which are subjected to tensile stresses along their length in vertical specimens and across their width in horizontal ones; furthermore, the greater elongation exhibited by vertical samples is consistent with the preferential <111> crystallographic orientation, which, in FCC metals, aligns favourably with the primary slip direction.

The effect of wobbling, instead, can be discussed considering the various strengthening mechanisms; it is well known that metallic materials are strengthened through five primary methods: dislocation strengthening (DS), work hardening strengthening (WHS), solid solution strengthening (SSS), precipitation strengthening (PS), and grain size strengthening (GSS) [42,47,48]. As 316L is not a solid solution strengthened alloy, solid solution strengthening (SSS) is not an active mechanism as well as the precipitation strengthening (PS) because 316L is not classified as a precipitation-hardenable alloy. Furthermore, although some studies have calculated the PS effect due to the presence of oxides using a modified version of the Orowan model [49], the micrometric size of oxides evidenced by SEM in these samples (Fig. 12) results in a marginal contribution, of only a few MPa. Consequently, only grain size strengthening (GSS) and dislocation strengthening (DS) can be considered as the dominant mechanisms affecting the overall mechanical performance.

Laser wobbling promoted both grain refinement and an increase in dislocation density, thereby enhancing the mechanical properties through GSS and DS. Although a slight increase in porosity was detected in the wobbling samples, the porosity levels remained minimal and did not significantly compromise the mechanical performance. Thus, the improvements in strength and ductility achieved through laser wobbling outweigh the minor drawbacks, highlighting its potential as an effective strategy for optimizing LP-DED components. Moreover, as already discussed in the previous sections, the positive effect of residual ferrite on mechanical properties must be considered; in fact, the lowest UTS is achieved in the W_V sample that is the only condition in which the IHT results in the complete reversion of this secondary phase.

Concerning GSS, using the Hall-Petch relation, the role of cell size,

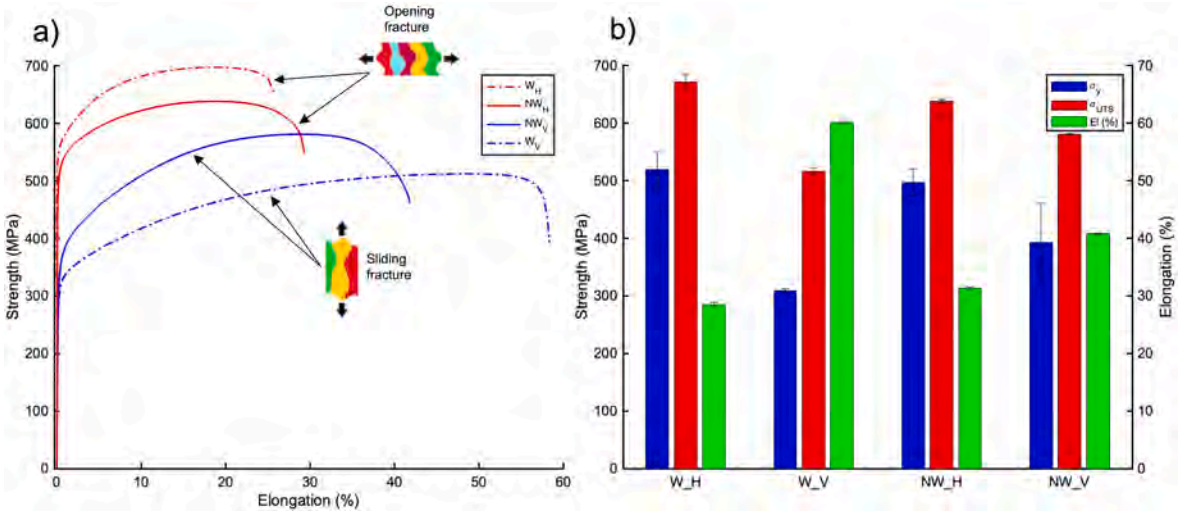

Fig. 13. Tensile test results of the analysed samples a) representative stress strain curves for each condition with a schematic representation of the fracture mode of the columnar grain characteristic of the LAM process and b) average values of YS, UTS and El. %.

whose walls are often decorated with high densities of dislocations, can be considered as contributing to strengthening, arising from forest dislocations [50,51]. Assuming the NW conditions, i.e. the conventional deposition strategy as a benchmark, grain size is crucial in enhancing the anisotropy between the deposition orientations.

It is interesting to note that when considering the deposition orientation individually, the yield behaviour is quite similar, suggesting that the oscillating process affects the material strain hardening capabilities. Focusing on the plastic behaviour of the alloy, in fact, this aspect become evident. Representative true stress-strain curves for both deposition orientations and processing conditions are illustrated in Fig. 14 using a log-log plot. In all cases, a two-stage work hardening behaviour is identified. This is expected for 316L stainless steel due to the change in dislocation slip mode with increasing plastic strain: planar slip dominates in the low-strain regime, known as the homogeneous strain region, while cross slip becomes prominent in the high-strain regime, referred to as the non-homogeneous strain hardening region.

The relationship between stress and strain during the plastic deformation of polycrystalline metallic materials can be described by the exponential strain hardening equation:

$$\sigma = K\varepsilon^{n}. \quad \text{(Eq. 7)}$$

where σ is the true stress, ε is the true plastic strain, K is the work hardening coefficient, and n is the work hardening exponent. For LP-DED 316L stainless steel, which exhibits a bilinear relationship, two exponents (n_1 and n_2) are necessary. In these samples, the loading direction significantly influences the work hardening capability. Horizontal depositions generally exhibit higher values than vertical ones, indicating enhanced work hardening capability and superior ductility. Wobbling only slightly affects the work hardening in vertical samples, with W_V and NW_V exhibiting similar n_1 values (0.91 and 0.90) and n_2 values (0.11 and 0.12). Conversely, samples in the horizontal orientation (W_H and NW_H) show greater variability in n_1 (1.03 and 1.23), while n_2 remains almost the same (0.09 and 0.12) for both. This outcome again must be reconducted to the IHT affecting the smaller cross sections which, inducing recrystallization, reduces the dislocation arrangement; hence, it is possible to state that the wobbling process has a positive effect increasing the initial strength in the homogeneous deformation domain.

The fracture surfaces of all samples, depicted in Fig. 15, confirm an absence of porosity and exhibit characteristic ductile fracture features. The vertical samples are characterized by a network of deep and small dimples with an average diameter of 3.2 μm, nested within larger dimples. In contrast, the fracture surfaces of horizontal samples feature smaller and more uniform dimples, averaging 1.3 μm in diameter, along with the occasional presence of cleavages. This variation in fracture behavior can be attributed to differences in grain boundary orientation (see schematic in Fig. 13a). The presence of elongated grains influences the fracture mode of the grain boundaries; in fact, when in the vertical samples the tension is parallel to the building direction, hence along the preferential grain growth, a sliding fracture is observed. Transferring this concept to horizontal depositions, when tension is applied transversely to the grains, the fracture mode changes to that of opening.

4. Conclusions

Based on the extensive microstructural and mechanical analyses conducted in this study, several key insights can be drawn regarding the impact of laser wobbling and deposition orientation on LP-DED 316L stainless steel samples.

- the use of the laser oscillation strategy generally produced numerous molten pools and thinner layers compared to raster scanning. This was due to lower dZ values and a larger apparent laser spot size, resulting in a higher surface-to-volume ratio for the molten pools and influencing the solidification conditions. However, for geometries with small cross-sections, deeper penetration was observed due to heat accumulation, leading to more pronounced remelting effects;
- the variation in the virtual laser spot size profoundly affected the microstructure. Convective flows in larger molten pools promoted dendritic grain fragmentation and overall refinement, highlighting a powerful method for controlling microstructural features during additive manufacturing;
- all samples exhibited strong anisotropy due to the presence of columnar grains. This anisotropy was even higher in samples built with the wobbling condition due to the intrinsic heat treatment it provides;
- the mechanical properties were primarily influenced by dislocation strengthening and grain size effects, with solidification cells and high dislocation densities playing crucial roles.

These findings advance the understanding of how process parameters in LP-DED can be strategically manipulated to tailor both

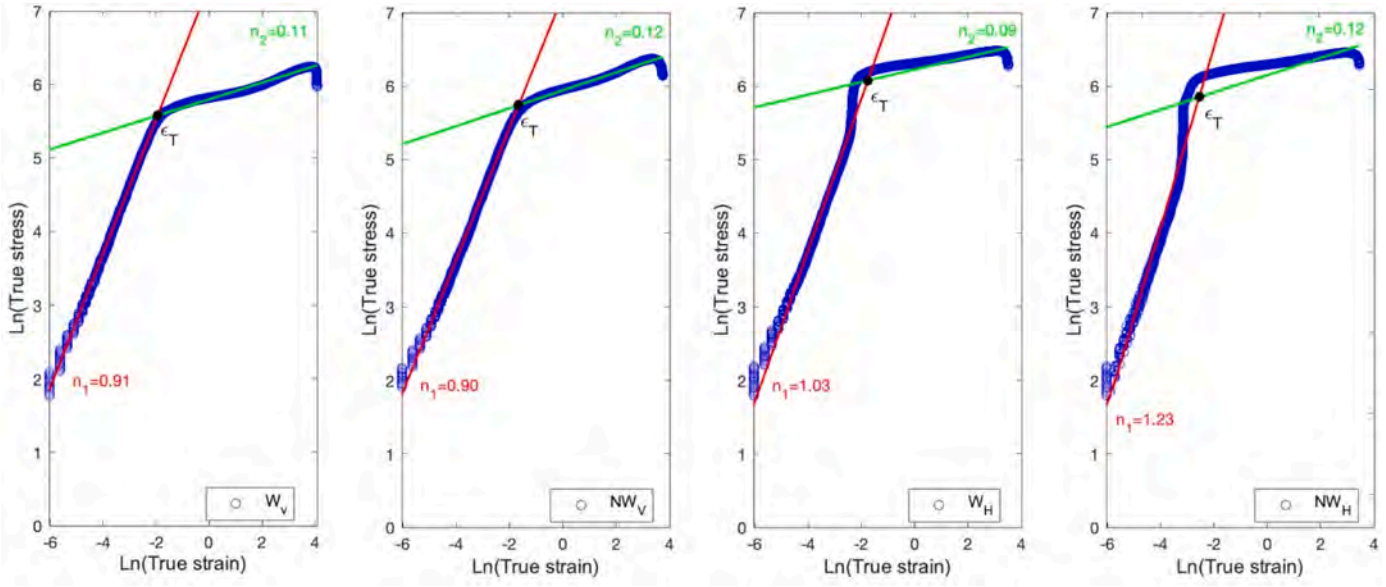

Fig. 14. Work hardening behaviour of the LP-DED 316L samples: true stress – true strain plots reporting the two-stage work hardening typical of 316L stainless steel.

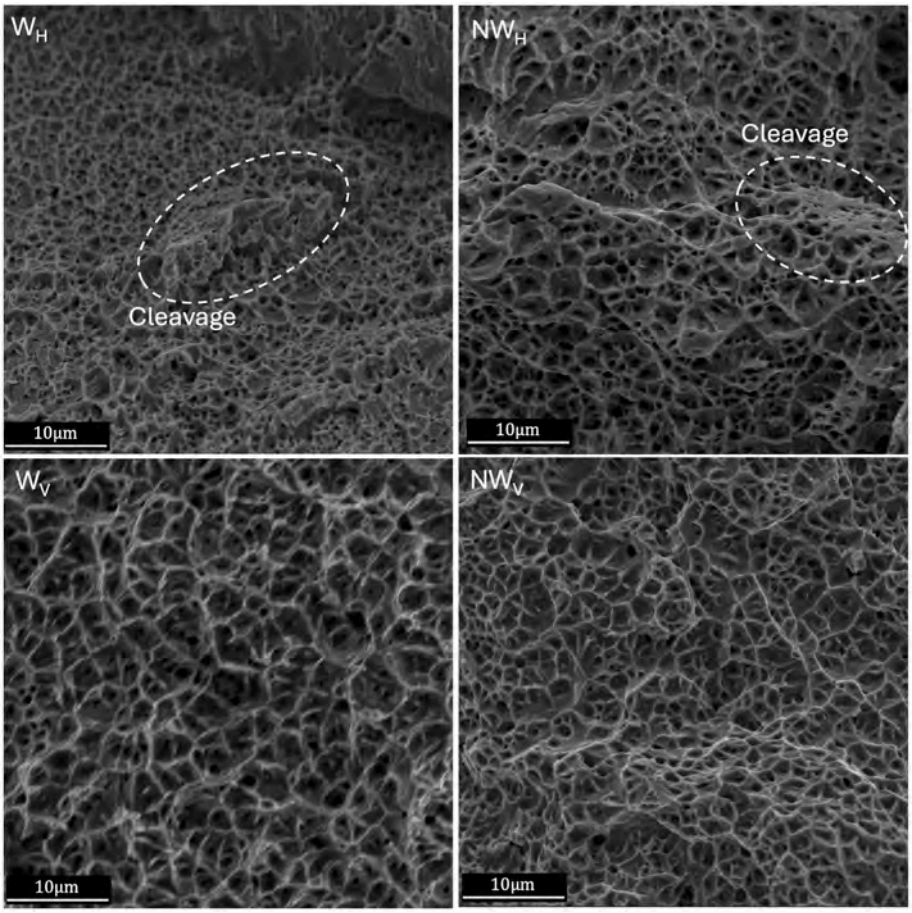

Fig. 15. Fracture surface of all condition: a-b) WH and NWH samples displaying traces of cleavages at the grain boundary; c-d) WV and NWV samples characterized by a full ductile fracture surface with lager and deeper dimples.

microstructure and mechanical performance. In particular, this work demonstrates that laser wobbling not only modifies melt pool dynamics but also offers a pathway toward designing additive manufacturing strategies that can engineer desired property gradients and microstructural architectures in metallic materials. Overall, this study contributes to the broader goal of optimizing additive manufacturing techniques for high-performance applications, particularly where fine control over microstructural anisotropy and mechanical properties is essential.

Data availability

Data will be made available on request.

Declaration of competing interest

The authors declare that there is no conflict of interest regarding the publication of this paper. No financial or personal relationships exist with other people or organizations that could inappropriately influence this work.

Acknowledgments

This research did not receive any specific grant from funding agencies in the public, commercial, or not-for-profit sectors.

Appendix A. Supplementary data

Supplementary data to this article can be found online at https://doi.org/10.1016/j.jmrt.2025.05.049.

References

[1] Sankaré MS F de Lima e S. Microstructure and mechanical behavior of laser additive manufactured AISI 316 stainless steel stringers. Mater Des mar. 2014;55:526–32. https://doi.org/10.1016/j.matdes.2013.10.016.
[2] Piscopo G, Atzeni E, Saboori A, Salmi e A. An Overview of the process mechanisms in the laser powder directed energy deposition. Appl Sci 2022;13(1):117. https://doi.org/10.3390/app13010117. dic.
[3] Félix-Martínez C, Ibarra-Medina J, Fernández-Benavides DA, Cáceres-Díaz LA, Alvarado-Orozco e JM. Effect of the parametric optimization and heat-treatment on the 18Ni-300 maraging steel microstructural properties manufactured by directed energy deposition. Int J Adv Manuf Technol 2021;115(11–12):3999–4020. https://doi.org/10.1007/s00170-021-07320-y. ago.
[4] Gibson I, Rosen D, Stucker e B. Additive manufacturing technologies: 3D printing. Rapid prototyping, and direct digital manufacturing. New York, NY: Springer New York; 2015. https://doi.org/10.1007/978-1-4939-2113-3.
[5] Wang Z, Palmer TA, Beese e AM. Effect of processing parameters on microstructure and tensile properties of austenitic stainless steel 304L made by directed energy deposition additive manufacturing. Acta Mater 2016;110:226–35. https://doi.org/10.1016/j.actamat.2016.03.019. mag.
[6] Li B, Wang B, Zhu G, Zhang L, Lu e B. Low-roughness-surface additive manufacturing of metal-wire feeding with small power. Materials lug. 2021;14(15):4265. https://doi.org/10.3390/ma14154265.
[7] Ghibaudo C, Wartbichler R, Marchese G, Clemens H, Ugues D, Biamino e S. Influence of focus offset on the microstructure of an intermetallic γ-TiAl based alloy produced by electron beam powder bed fusion. J Manuf Process mar. 2023;89:132–41. https://doi.org/10.1016/j.jmapro.2023.01.061.
[8] Miller D, Deckard C, Williams e J. Variable beam size SLS workstation and enhanced SLS model. Rapid Prototyp J gen. 1997;3(1):4–11. https://doi.org/10.1108/13552549710169237.
[9] Aversa A, et al. Productivity enhancement in directed energy deposition: the oscillating scanning strategy approach. Met Mater Int lug. 2023;29(7):2040–51. https://doi.org/10.1007/s12540-022-01356-9.
[10] Gong M, Meng Y, Zhang S, Zhang Y, Zeng X, Gao e M. Laser-arc hybrid additive manufacturing of stainless steel with beam oscillation. Addit Manuf 2020;33:101180. https://doi.org/10.1016/j.addma.2020.101180. mag.
[11] Huang T-Y, Cheng C-W, Lee A-C, Chang T-W, Tsai e M-C. Influence of wobble-based scanning strategy on surface morphology of laser powder bed-fabricated

permalloy. Materials mar. 2023;16(5):2062. https://doi.org/10.3390/ma16052062.
[12] Shah LH, Khodabakhshi F, Gerlich e A. Effect of beam wobbling on laser welding of aluminum and magnesium alloy with nickel interlayer. J Manuf Process gen. 2019;37:212–9. https://doi.org/10.1016/j.jmapro.2018.11.028.
[13] Kuryntsev SV, Gilmutdinov e A Kh. The effect of laser beam wobbling mode in welding process for structural steels. Int J Adv Manuf Technol dic. 2015;81(9–12):1683–91. https://doi.org/10.1007/s00170-015-7312-y.
[14] Voropaev AA, et al. Influence of laser beam wobbling parameters on microstructure and properties of 316L stainless steel multi passed repaired parts. Materials 2022;15(3):722. https://doi.org/10.3390/ma15030722. gen.
[15] de Oliveira CC, Pereira M, da Silveira CA, Dutra MK, Amaral e C. Effect of wobble parameters on microwelding bead formation of AISI 316L stainless steel. J Laser Appl 2023;35(4):042025. https://doi.org/10.2351/7.0001123. set.
[16] Aversa A, et al. The role of Directed Energy Deposition atmosphere mode on the microstructure and mechanical properties of 316L samples. Addit Manuf 2020;34:101274. https://doi.org/10.1016/j.addma.2020.101274. ago.
[17] Zhang K, Wang S, Liu W, Shang e X. Characterization of stainless steel parts by laser metal deposition shaping. Mater Des mar. 2014;55:104–19. https://doi.org/10.1016/j.matdes.2013.09.006.
[18] Santecchia E, et al. Microstructural features induced by the Gaussian laser beam shape on 316L stainless steel thin-walled samples fabricated by directed energy deposition. Prog. Addit. Manuf. 2025. https://doi.org/10.1007/s40964-025-01028-1.
[19] Li S-H, Zhao Y, Kumar P, Ramamurty e U. Effect of initial dislocation density on the plastic deformation response of 316L stainless steel manufactured by directed energy deposition. Mater Sci Eng, A ago. 2022;851:143591. https://doi.org/10.1016/j.msea.2022.143591.
[20] Lee S, Ghiaasiaan R, Gradl PR, Shao S, Shamsaei e N. Additively manufactured 316L stainless steel via laser powder directed energy deposition (LP-DED): mechanical properties at cryogenic and elevated temperatures. Int J Fatig 2024;182:108197. https://doi.org/10.1016/j.ijfatigue.2024.108197. mag.
[21] Zięţala M, et al. The microstructure, mechanical properties and corrosion resistance of 316L stainless steel fabricated using laser engineered net shaping. Mater Sci Eng, A nov. 2016;677:1–10. https://doi.org/10.1016/j.msea.2016.09.028.
[22] Yadollahi A, Shamsaei N, Thompson SM, Seely e DW. Effects of process time interval and heat treatment on the mechanical and microstructural properties of direct laser deposited 316L stainless steel. Mater Sci Eng, A 2015;644:171–83. https://doi.org/10.1016/j.msea.2015.07.056. set.
[23] Ma M, Wang Z, Zeng e X. A comparison on metallurgical behaviors of 316L stainless steel by selective laser melting and laser cladding deposition. Mater Sci Eng, A feb. 2017;685:265–73. https://doi.org/10.1016/j.msea.2016.12.112.
[24] Xu K, Li B, Jiang e C. Adjusting microstructure and improving mechanical property of additive manufacturing 316L based on process optimization. Mater Sci Eng, A apr. 2023;870:144824. https://doi.org/10.1016/j.msea.2023.144824.
[25] B09 Committee, Test method for density of powder metallurgy (PM) materials containing less than two percent porosity. doi: 10.1520/B0311-22.
[26] Guo D, et al. Solidification microstructure and residual stress correlations in direct energy deposited type 316L stainless steel. Mater Des 2021;207:109782. https://doi.org/10.1016/j.matdes.2021.109782. set.
[27] E28 Committee, «Test methods for tension testing of metallic materials», ASTM International. doi: 10.1520/E0008_E0008M-24.
[28] Griffith ML, et al. Understanding thermal behavior in the LENS process. Mater Des giu. 1999;20(2–3):107–13. https://doi.org/10.1016/S0261-3069(99)00016-3.
[29] Zheng B, et al. On the evolution of microstructure and defect control in 316L SS components fabricated via directed energy deposition. Mater Sci Eng, A 2019;764:138243. https://doi.org/10.1016/j.msea.2019.138243. set.
[30] Selcuk C. Laser metal deposition for powder metallurgy parts. Powder Metall 2011;54(2).
[31] Saboori A, et al. An investigation on the effect of powder recycling on the microstructure and mechanical properties of AISI 316L produced by Directed Energy Deposition. Mater Sci Eng, A 2019;766:138360. https://doi.org/10.1016/j.msea.2019.138360. ott.
[32] Helmer HE, Körner C, Singer e RF. Additive manufacturing of nickel-based superalloy Inconel 718 by selective electron beam melting: processing window and microstructure. J Mater Res 2014;29(17):1987–96. https://doi.org/10.1557/jmr.2014.192. set.
[33] Gäumann M, Henry S, Cléton F, Wagnière J-D, Kurz e W. Epitaxial laser metal forming: analysis of microstructure formation. Mater Sci Eng, A nov. 1999;271(1–2):232–41. https://doi.org/10.1016/S0921-5093(99)00202-6.
[34] Jiang Z, et al. Grain refinement and laser energy distribution during laser oscillating welding of Invar alloy. Mater Des 2020;186:108195. https://doi.org/10.1016/j.matdes.2019.108195. gen.
[35] Zhao J, Jiang P, Geng S, Guo L, Wang Y, Xu e B. Experimental and numerical study on the effect of increasing frequency on the morphology and microstructure of aluminum alloy in laser wobbling welding. J Mater Res Technol nov. 2022;21:267–82. https://doi.org/10.1016/j.jmrt.2022.09.008.
[36] Cui S, Shi Y, Sun K, Gu e S. Microstructure evolution and mechanical properties of keyhole deep penetration TIG welds of S32101 duplex stainless steel. Mater Sci Eng, A gen. 2018;709:214–22. https://doi.org/10.1016/j.msea.2017.10.051.
[37] Odnobokova M, Yanushkevich Z, Kaibyshev R, Belyakov e A. On the strength of a 316L-type stainless steel subjected to cold or warm rolling followed by annealing. Materials 2020;13(9):2116. https://doi.org/10.3390/ma13092116. mag.
[38] Odnobokova M, Belyakov A, Kaibyshev e R. «Development of nanocrystalline 304L stainless steel by large strain cold working», metals apr. 2015;5(2):656–68. https://doi.org/10.3390/met5020656.
[39] Sun Z, Tan X, Tor SB, Yeong e WY. Selective laser melting of stainless steel 316L with low porosity and high build rates. Mater Des ago. 2016;104:197–204. https://doi.org/10.1016/j.matdes.2016.05.035.
[40] Saeidi K, Gao X, Zhong Y, Shen e ZJ. Hardened austenite steel with columnar subgrain structure formed by laser melting. Mater Sci Eng, A feb. 2015;625:221–9. https://doi.org/10.1016/j.msea.2014.12.018.
[41] Weng F, Gao S, Jiang J, Wang J, Guo e P. A novel strategy to fabricate thin 316L stainless steel rods by continuous directed energy deposition in Z direction. Addit Manuf 2019;27:474–81. https://doi.org/10.1016/j.addma.2019.03.024. mag.
[42] Reitz W. «A review of: "welding metallurgy and weldability of stainless steel". Mater Manuf Process apr. 2006;21(2):219. https://doi.org/10.1080/10426910500476747. 219.
[43] Li D, Lu S, Li D, Li e Y. Investigation of the microstructure and impact properties of the high nitrogen stainless steel weld. Acta Metall Sin 2013;49(2):129. https://doi.org/10.3724/SP.J.1037.2012.00514.
[44] Waheed K Amany e AF. «EUROPEAN ACADEMIC RESEARCH», correl. Corros. Ferrite number 316L stainl. Steels Deposited Carbon Steel Aged 550° C 2019;VII(3).
[45] Li K, Li D, Liu D, Pei G, Sun e L. Microstructure evolution and mechanical properties of multiple-layer laser cladding coating of 308L stainless steel. Appl Surf Sci giu. 2015;340:143–50. https://doi.org/10.1016/j.apsusc.2015.02.171.
[46] A01 Committee, Specification for stainless steel bars and shapes for use in boilers and other pressure vessels. doi: 10.1520/A0479_A0479M-23A.
[47] Kok Y, et al. Anisotropy and heterogeneity of microstructure and mechanical properties in metal additive manufacturing: a critical review. Mater Des feb. 2018;139:565–86. https://doi.org/10.1016/j.matdes.2017.11.021.
[48] Röttger A, Geenen K, Windmann M, Binner F, Theisen e W. Comparison of microstructure and mechanical properties of 316 L austenitic steel processed by selective laser melting with hot-isostatic pressed and cast material. Mater Sci Eng, A dic. 2016;678:365–76. https://doi.org/10.1016/j.msea.2016.10.012.
[49] Dadé M, et al. Influence of microstructural parameters on the mechanical properties of oxide dispersion strengthened Fe-14Cr steels. Acta Mater 2017;127(apr):165–77. https://doi.org/10.1016/j.actamat.2017.01.026.
[50] Voisin T, et al. New insights on cellular structures strengthening mechanisms and thermal stability of an austenitic stainless steel fabricated by laser powder-bed-fusion. Acta Mater 2021;203:116476. https://doi.org/10.1016/j.actamat.2020.11.018. gen.
[51] Li Z, He B, Guo e Q. Strengthening and hardening mechanisms of additively manufactured stainless steels: the role of cell sizes. Scr Mater mar. 2020;177:17–21. https://doi.org/10.1016/j.scriptamat.2019.10.005.